Applied Surface Science 470 (2019) 1122–1129

Contents lists available at ScienceDirect

Applied Surface Science

journal homepage: www.elsevier.com/locate/apsusc

Full Length Article

Drift-insensitive distributed calibration of probe microscope scanner in nanometer range: Real mode

Rostislav V. Lapshin*

Solid Nanotechnology Laboratory, Institute of Physical Problems, Zelenograd, Moscow 124460, Russian Federation
Department of Integral Electronics and Microsystems, National Research University of Electronic Technology, Zelenograd, Moscow 124498, Russian Federation

ARTICLE INFO

Keywords:
STM
AFM
SPM
Scanner
Calibration
Drift
Creep
Nonlinearity
Nonorthogonality
Crosstalk coupling
Graphite
HOPG
Feature-oriented scanning
FOS
Counter-scanned images
Nanometrology
Surface characterization
Nanotechnology

ABSTRACT

A method is described intended for distributed calibration of a probe microscope scanner consisting in a search for a net of local calibration coefficients (LCCs) in the process of automatic measurement of a standard surface, whereby each point of the movement space of the scanner can be defined by a unique set of scale factors. Feature-oriented scanning (FOS) methodology is used to implement the distributed calibration, which permits to exclude *in situ* the negative influence of thermal drift, creep and hysteresis on the obtained results. The sensitivity of LCCs to errors in determination of position coordinates of surface features forming the local calibration structure (LCS) is eliminated by performing multiple repeated measurements followed by building regression surfaces. There are no principle restrictions on the number of repeated LCS measurements. Possessing the calibration database enables correcting in one procedure all the spatial distortions caused by nonlinearity, nonorthogonality and spurious crosstalk couplings of the microscope scanner piezomanipulators. To provide high precision of spatial measurements in nanometer range, the calibration is carried out using natural standards – constants of crystal lattice. The method allows for automatic characterization of crystal surfaces at room temperature. The method may be used with any kind of scanning probe microscope (SPM).

1. Introduction

Usually, a probe microscope scanner is characterized by three calibration coefficients K_x, K_y, K_z representing sensitivities of X, Y, Z piezomanipulators, respectively (to take into consideration a possible nonorthogonality of X, Y piezomanipulators, an obliquity angle should be additionally determined) [1–4]. Because of piezomanipulators' nonlinearity [5–7] and spurious crosstalk couplings, the probe microscope scanner may be described by the above coefficients only near the origin of coordinates, where the influence of the distortion factors is insignificant. As moving away from the origin of coordinates, the topography measurement error would noticeably increase reaching the utmost value at the edge of the scanner field (see Section 2.5).

The problem may be solved by using a distributed calibration, which implies determining three local calibration coefficients (LCCs) K_x, K_y, K_z for each point of the scanner movement space, which can be thought of as scale factors for axes x, y and z, respectively [8–13]. A reference surface used for calibration should consist of elements, called hereinafter features, such that the distances between them or their sizes are known with a high precision. The corrected coordinate of a point on the distorted image of an unknown surface is obtained by summing up the LCCs related to the points of the movement trajectory of the scanner [11].

Both lumped and distributed calibration of the probe microscope scanner should be carried out by the data where distortions caused by drifts (thermal drifts of instrument components plus creeps of piezomanipulators) are eliminated. Otherwise, the measurements will have large errors [2,3,12,14,15]. In the present work, to eliminate the negative influence of thermal drift and creep on the distributed calibration results, the methods are used of feature-oriented scanning (FOS) [14] and of counter-scanning [15].

This article completes the series of three articles dedicated to the FOS-based distributed calibration. In the first article [11] of the series, the suggested calibration procedure has been described in detail and

* Correspondence to: Solid Nanotechnology Laboratory, Institute of Physical Problems, Zelenograd, Moscow 124460, Russian Federation.
E-mail address: rlapshin@gmail.com.

https://doi.org/10.1016/j.apsusc.2018.10.149
Received 29 August 2018; Accepted 16 October 2018
Available online 17 October 2018
0169-4332/

also the working formulae have been derived for correction of the scan of an arbitrary surface. The second article [12] of the series is devoted to the virtual mode of the distributed calibration. The virtual mode implies that, instead of measurement of the real surface of a standard, the calibration program performs the "measurement" of an image of the standard surface, which has been obtained earlier during conventional scanning. The virtual mode is intended for simulation of calibration process and validation of analytical solutions found in the first article of the series. The virtual mode allows significant acceleration of the development and debugging of the real mode. The real mode being the subject of the present investigation implies that the distributed calibration of the scanner is performed by graphite crystal lattice in real time. The real mode permits to acquire the calibration database (CDB) that completely characterizes the piezoscanner of the microscope in use in the lateral plane. A distributed calibration by the suggested method including calibration in the vertical plane is planned to implement at the next stage of the method development.

2. Experimental results

Distributed calibration of scanner of the probe microscope Solver™ P4 (NT-MDT Co., Russia) in the real mode was carried out by atomic topography of basal plane (0001) of highly oriented pyrolytic graphite (HOPG) monocrystal (Research Institute of Graphite, Russia). HOPG's mosaic spread angle makes 0.8° (graphite density 2.24 g/cm^3, purity 99.999%). In order to minimize thermal deformation of the sample, a graphite crystal of small dimensions 2 × 4 × 0.3 mm was used. Three adjacent carbon atoms (or interstices) forming an equilateral triangle ABC were selected as a local calibration structure (LCS) [11]. According to the neutron diffraction method, the lattice constant a (actually, the length of a side of the ABC triangle) of a natural graphite single crystal makes 2.464 ± 0.002 Å (relative error ± 0.08%) [16].

Graphite surface topography was obtained by scanning tunneling microscopy (STM). With microscope Solver, scanning is carried out by moving a sample relative to a fixed tip. As the tip, a mechanically cut NiCr wire with diameter 0.3 mm was used. To protect the microscope against floor vibrations, a passive vibration isolation system was employed. Moreover, the microscope was housed under a thermoinsulation hood, which also served as an absorber of external acoustic disturbances. Neither constant temperature nor constant humidity were maintained in the laboratory room where the calibration was implemented. The typical noise level of the tunneling current in the course of the measurements made about 20 pA (peak-to-peak).

The microscope scanner is a piezotube having four electrodes on the outer side and a solid grounded electrode inside. The piezotube was fabricated by sintering piezoceramic powder mixture similar to PZT-5A (lead zirconate titanate Pb(Zr, Ti)O_3, ELPA Co., Russia). The maximal unipolar voltage applied to the piezotube X, Y electrodes makes 150 V. Between the electrodes of the manipulators of the same name, the tube piezoceramic is polarized in mutually opposite directions. X, Y DACs have capacity of 16 bits.

During the raster scanning, the probe movement velocity at the retrace sweep was set the same as at the forward trace. Immediately before every raster scanning, a "training" of the scanner was carried out [15]. The scanner training is a repeated movement along the first line, which allows to decrease creep at the beginning of the scan [17]. While training, the actual scanning velocity was also determined.

2.1. Selection of a calibration area on the surface of a standard

Since the whole scanning field of the microscope used makes about 2 × 2 μm and the typical sizes of atomically smooth regions suitable for calibration on the surface of the graphite sample did not usually exceed 450 × 450 nm, the distributed calibration was carried out by parts. First, a trial scanning of the whole field was conducted, and then plane smooth typically 300 × 300 nm size regions with no visible defects were selected therein.

The above scale is set based on the following considerations. First, nanodimensional surface defects, whose presence is undesirable, are still distinguishable with this scale. Second, with the typical net step of 5–25 nm, the time of calibration by a region of such sizes will not be too long. Third, around the region, a surface area suitable for calibration can still be reserved with the sizes that allow the probe to stay within its limits even after being shifted by the end of calibration due to drift.

After the calibration had been completed at each of the selected regions, the whole scanner field was shifted to an adjacent area on the crystal or the pyrographite crystal was cleft. Periodical graphite cleaving not only permits to refresh the surface but also to reduce the errors resulted from small variations of the lattice constant and variations of angles between the crystallographic directions during the subsequent averaging. Those errors arise from imperfections relating to the standard itself (see Section 2.6).

Since during the time of calibration, which may take up from several hours to several days, the standard surface is shifted significantly within the field of view of the microscope because of drift, the whole scanner field does not require to be shifted frequently. The calibration can be continued at either the shifted old surface region or at a new region that appeared in the field of view of the instrument. The operations described above are repeated until most of the scanner field is calibrated.

Fig. 1 shows the areas of distributed calibrations within the scanner field. The areas consist of red points designating the LCS positions for which LCCs have been found. The sizes of the areas are determined by the net step and the number of net nodes. For example, outlined with a single frame is the area 73 × 73 Å calibrated by net of 31 × 32 nodes having the step as small as 8 positions (about 2.44 Å). Outlined with a double frame is the area 396 × 402 nm calibrated by net of 37 × 39 nodes having the step as large as 361 positions (about 11 nm). Some areas overlap with each other. The triple frame outlines one of the areas where such overlap takes place. In areas like this, it is possible to analyze relative variations of the constant lattice of the applied HOPG crystal (see Section 2.6). All the calibrations in Fig. 1 have been performed with the Z manipulator of the scanner extended to the middle of its range.

The presence of some areas not covered by calibration in Fig. 1 is not critical as regression (averaging) surfaces will be drawn through the obtained LCCs using the least-squares method (see Section 2.4). The suggested method allows conducting repeated and additional calibrations in any area of the scanner field as many times as needed. The obtained data are simply added to the common calibration database.

One placement of the STM head and one tip were sufficient for 1.5 weeks of practically ceaseless operation. That period is restricted by the tip lifetime, which is determined by the slow growth of native oxide layer [18]. The tip surface oxidation causes an increase in the tip curvature radius as well as in the noise level of the tunneling current, which leads to the loss of atomic resolution at a certain moment. The increase of the curvature radius is caused by tip material volume increase during oxidation. The increase in noise level is caused by the growing number of water molecules adsorbed by hydrophilic oxide [19] while working in the air; another reason of the noise is because the oxide is mechanically instable [18].

Despite of large amount of scanning typical of FOS [14,15], the calibration under consideration implies less mechanical wear of the tip than usual provided that the bias voltage and the tunneling current have the proper values. The fact is that most of the time the tip is held within the boundaries of atomically smooth area of the standard, so there is a low possibility of the tip collision with highly prominent topography asperities. Moreover, the tip moves over the surface with a small step since the microscope operates near its resolution limit; the tip moves at small distances and with low speed in order to prevent large creep. All these factors decrease the probability of mechanical interaction between the tip and the surface that could result in notable tip

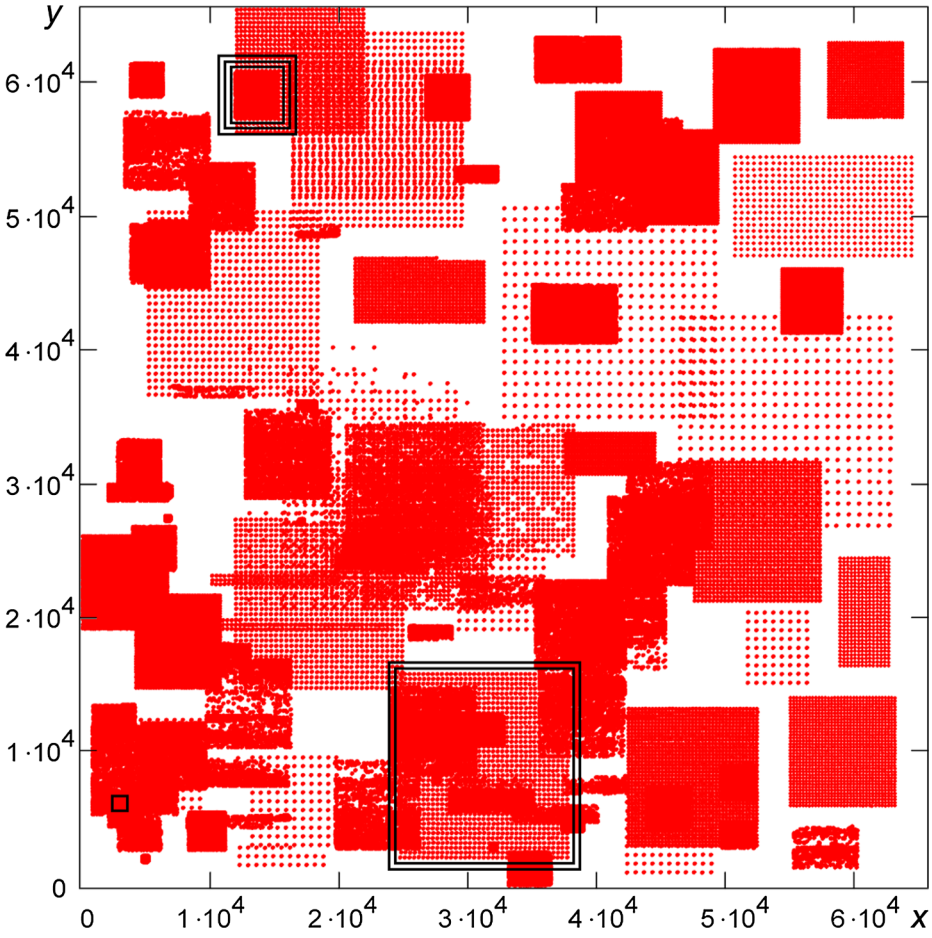

Fig. 1. Areas covered by distributed calibrations. The red points "•" designate the LCS positions for which LCCs were found. The *x* and *y* axes are graduated in lateral positions of the scanner. The whole scanner field is approximately equal to 2 × 2 μm. The calibrations have been conducted at the position of the scanner Z manipulator extended to the middle of its range.

wear (blunting).

The change in the shape of the tip caused by the above reasons has little effect on the accuracy of the calibration, since all atoms/interstices in the apertures and segments are distorted by the tip in the same way, and therefore there is no change in the relative distances between atoms/interstices in the LCS. Moreover, unlike calibration by micro-objects, the interaction of the complex side surface of the probe with the standard surface is completely absent during calibration by atoms of a crystal lattice; only the probe apex, which is actually a small cluster of several atoms having a well defined form, is involved in the interaction.

Graphite cleavage between the calibrations was carried out seldom, approximately once in 2–3 months. In case of failure to get a stable image of good quality by using the constant-current mode, the constant-height mode was applied for calibration in the lateral plane.

2.2. Measurement parameters and modes

Before the calibration started, the scanner's Z manipulator was moved to the middle of its range by using a coarse approach stage whereupon it was held near this position during all the time of calibration. Since the drift in the vertical plane is tens of times less than the drift in the lateral plane, control commands were applied to the Z manipulator rarely.

The STM measurements of the standard surface were conducted under ambient conditions at room temperature after the instrument had been warmed up [20,21] in active state for hours. The active state implies periodical attachment of the microscope probe to the carbon atom [11,14] located near the start position (1st net node) of the distributed calibration. Beside warming up, the attachment allows for monitoring the instrument state – noise level, resolution, and drift velocity. Thus, by observing the change in drift velocity in this mode, the termination moment of the warming-up stage can be determined.

The calibration results for each area were put into the common calibration database. The calibration was carried out either by LCS consisting of carbon atoms or by LCS consisting of interstices [12] depending on which LCS was closer to the current net node. Such approach allows avoiding calibration interruption in case the image of the atomic surface becomes accidentally inverted. Moreover, the probe path from the current net node into the A feature position becomes shorter.

Fig. 2 shows the initial net (net nodes are designated as "+"), the locations of LCSs detected during calibration (designated as "•") as well as movement trajectory of the probe from feature to feature (solid line). The movements within the local rasters while scanning the apertures [11] and segments [11] are not shown at the trajectory. In Fig. 2(a), the case of calibration with the small step ≈2.44 Å (8 scanner positions) is presented and in Fig. 2(b), the case of calibration with the large step ≈11 nm (361 scanner positions) is presented. The calibration area size in Fig. 2(a) is 73 × 73 Å (in Fig. 1, the area is outlined with a single frame); in Fig. 2(b) the size is 396 × 402 nm (in Fig. 1, the area is outlined with a double frame). In both cases, the measurements were taken in the constant-current mode. According to the trajectory given in Fig. 2(a), the microscope probe is continually shifted aside from the nodes of the initial net due to some drift (cp. with Fig. 2 in Ref. [12]). Fig. 2(b) clearly shows that the movements by the net nodes are performed in full compliance with the trajectory shown in Fig. 1(a) of Ref. [11].

The waiting time after moving to the next net node was 3 s for the calibration shown in Fig. 2(a) and 11 s for the calibration in Fig. 2(b). The number of probe attachments following the pause usually made 2–7 with the regular scanning and 2–4 with the counter-scanning. As an example, three consecutive probe attachments PA1, PA2, PA3 to the

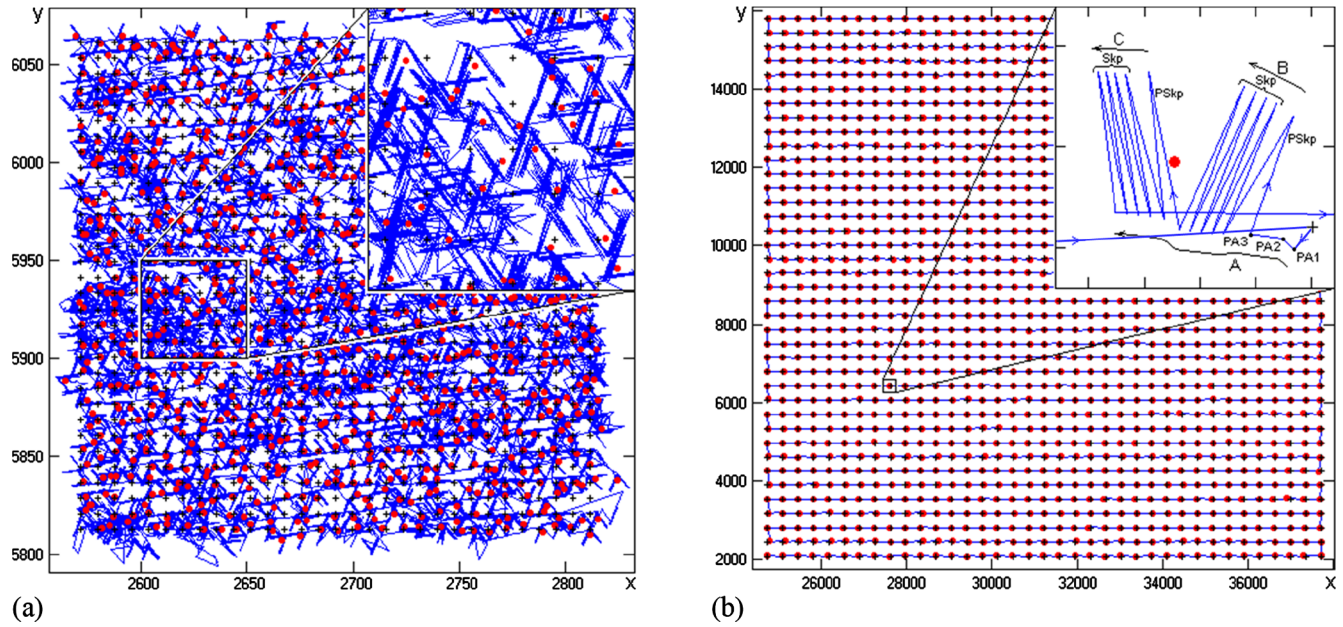

Fig. 2. Distributed calibration within area (a) 73 × 73 Å (31 × 32 nodes), (b) 396 × 402 nm (37 × 39 nodes) with step (a) 2.44 Å (8 positions), (b) 11 nm (361 positions). The number of detected LCSs (a) 992, (b) 1443 ("•" designates LCS locations). Measurement mode: STM, constant-current, U_{tun} = 50 mV, I_{tun} = 856 pA. During the time (a) 23.8 h, (b) 57.3 h of calibration, (a) 24174, (b) 48365 attachments were carried out; (a) 2429, (b) 3010 apertures and (a) 22750, (b) 31569 segments were scanned. Mean lateral drift velocity made (a) 0.147 Å/s, (b) 0.149 Å/s. The *x* and *y* axes are graduated in lateral positions of the scanner. The data correspond to the position of scanner Z manipulator moved to the middle of its range.

feature A located near one of the net nodes are shown in the inset of Fig. 2(b). The attachment PA1 is the first attachment performed after moving the tip into a net node. The attachment PA2 is carried out by the results of scanning-recognition of an aperture with the center in point PA1. The attachment PA3 is carried out by the results of scanning-recognition of the segment of feature A with the center in point PA2. The total number of probe attachments to feature A during the calibration within the area in Fig. 2(a) was 24174, within the area in Fig. 2(b) – 48365.

In the course of the measurements, the aperture size was 31 × 31 points (9.2 × 8.8 Å approx.), the segment size was 21 × 21 points (6.1 × 5.9 Å approx.). The scanning speed in aperture/segment was set as 592 Å/s for calibration presented in Fig. 2(a) and as 465 Å/s for calibration presented in Fig. 2(b). During calibration, 2429 apertures and 22750 segments were scanned in the area shown in Fig. 2(a), 3010 apertures and 31569 segments – in the area shown in Fig. 2(b). The number of averagings of topography height in a raster point while scanning the apertures and the segments was 15 and 25 for calibrations in Fig. 2(a) and in Fig. 2(b), respectively. Only one of the LCSs detected in the aperture, the one nearest to the current net node, was used for calibration (LCS ABC, see Fig. 3(a) in Ref. [11]).

In the inset to Fig. 2(b), PSkp and Skp are preskipping and skipping cycles, respectively (for the sake of clarity, the probe movements in these cycles are shown slightly idealized). The number of consecutive skipping Skp cycles was set to 4. Before the skipping at least one preskipping PSkp cycle was performed [14]. The required number of preskipping cycles is set automatically. Preskipping is an idle (tuning) skipping required for the relative distance measurement process to reach its operating condition (cp. trajectories of PSkp and Skp in the inset in Fig. 2(b)). Movement velocity between features was set to 22 Å/s in both calibrations presented in Fig. 2. LCS measurements were performed at moments when the lateral drift velocity did not exceed 0.05 Å/s by module. In the inset to Fig. 2(b), the arrows near the A, B, and C features show the drift direction. Mean lateral drift velocity $|\bar{v}_{xy}|$ (thermal drift + creep) during calibration by the area in Fig. 2(a) made 0.147 Å/s, by the area in Fig. 2(b) – 0.149 Å/s. The number of feature losses fixed during calibration by the area in Fig. 2(a) was 17, by the area in Fig. 2(b) – 68.

While conducting the measurements, it was found that the larger is the speed of probe lateral movement relative to the surface in aperture/segment or at the skipping, the stronger is the creep excited during this movement. The strong creep, in its turn, requires setting a longer pause and leads to a greater number of attachments inserted automatically after the pause. On the other hand, the movement velocity should not be set too small since too slow movement leads to low calibration productivity and to higher probability of feature loss in case of a strong drift. The above scan and skipping velocities have been found experimentally and are optimal for this particular microscope.

The larger the step of the initial net, the stronger disturbance is introduced into the calibration process at the moment of movement from the current node to the next one and the longer time is required for this disturbance relaxation. The method retained full functionality while conducting distributed calibrations with the step of the initial net up to 500 nm. Larger steps were not tested because of lack of suitable regions of large enough sizes on the standard surface.

2.3. Actions of the algorithm when the measurand goes out of the tolerance limits

Because of defects and mostly because of all kinds of instabilities, the measured LCS sizes may not fall into the acceptance limits defined before the calibration (usually ± 8% for linear dimensions and ± 5° for angular ones). In such situation, the calibration program, in accordance with the operator's choice, can act on the following two scenarios. On the first one, after all the possibilities of rescans have been exhausted, the algorithm fixes a surface defect in this place, and after that it continues calibration in the next net node. In this case, LCCs for some scanner positions will be absent in the obtained CDB.

According to the second scenario, the algorithm moves the probe again into the current net node where a new attempt is made to find LCCs within the neighborhood of this node. The number of such returns to the current node depends on particular measurement conditions at the given moment of time. This state of calibration process is represented as loops on the trajectory. After some time, either the measurement conditions change so allowing to obtain LCS with parameters

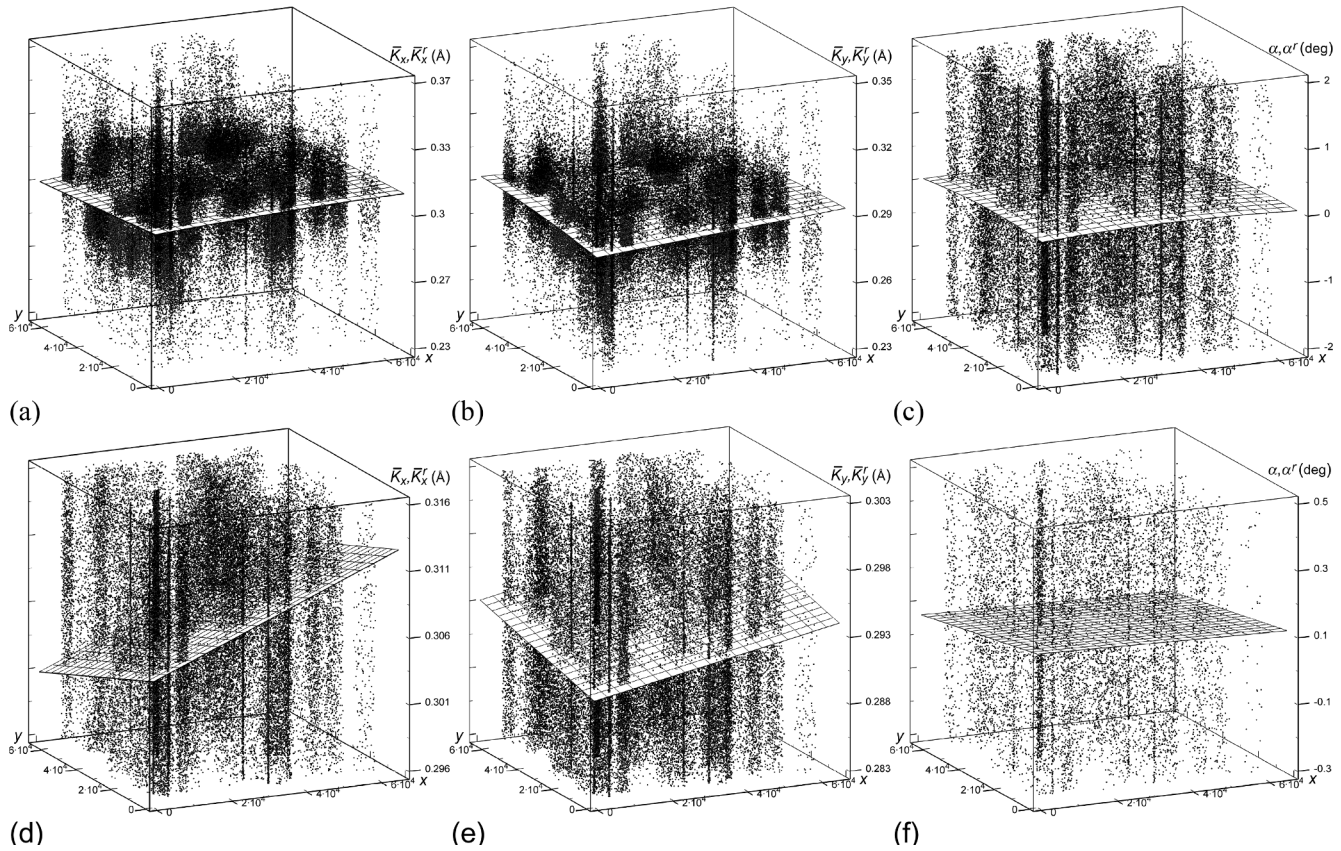

Fig. 3. Regression surfaces of 2nd order (upper row) and 1st order (lower row) drawn through (a), (d) LCCs $\bar{K}_x$, (b), (e) LCCs $\bar{K}_y$, and (c), (f) local obliquity angles α of the obtained CDB. The vertical scale of the surfaces (d)–(f) is intentionally stretched out so to better see the slope of those surfaces. CDB size makes 106683 LCSs. The x and y axes are graduated in lateral positions of the scanner. The data correspond to the position of scanner Z manipulator moved to the middle of its range.

within the limits of the set tolerances, or, due to drift, some other area of the standard surface with no defects gets into the current node surroundings. The results shown in Fig. 1 were mainly obtained with the use of the second scenario.

2.4. Calibration database, constructing regression surfaces

Figs. 3(a)–(c) show the sought 2nd order regression surfaces built by LCCs of the joint CDB of the piezoscanner. To facilitate the analysis, Figs. 3(a)–(c) have the same vertical scales as Figs. 3(a)–(c) in Ref. [12], where the regression surfaces were obtained in the virtual mode. The joint CDB contains information about $n = 106683$ LCSs. Because of disturbing factors and, to a much lesser extent, defects of the standard, some LCCs and local obliquity angles have noticeable deviations (within the limits of the tolerances set at the calibrations) from the expected values. Therefore, before being used the CDB was thinned out discarding such values. In order to perform the thinning as efficiently as possible, first the expected values should be obtained as close to the true values as possible. To do so, the method described in Ref. [15] can be employed for example.

Mean values of LCCs $<\bar{K}_x> = 0.304$ Å, $<\bar{K}_y> = 0.290$ Å and obliquity angle $<\alpha> = 0.1^\circ$ were found near the scanner's origin of coordinates (area of analysis 500 × 500 nm) using the regression surfaces. Indication that the real mode calibration is done correctly, is the proximity of the mean values of LCCs to each other [15] and to the initial coefficients $\Delta_x = 0.306$ Å, $\Delta_y = 0.307$ Å as well as the proximity of the mean obliquity angle to $\alpha = 0.4^\circ$ [15]. Note that the coefficients Δ_x, Δ_y and the obliquity angle α were obtained near the scanner's origin of coordinates during calibration by the image which distortions induced by thermal drift and creep had been eliminated [15].

Because of the appreciable difference between $<\bar{K}_x>$ and $<\bar{K}_y>$ (4.6% instead of 0.3% in Ref. [15]), it could be assumed that for some reason the y drift component was not fully corrected in the course of the distributed calibration. However, after switching the direction of the fast scan in apertures and in segments from x to y, exactly the same values were obtained. In order to finally eliminate any doubts concerning the differences in the coefficients, the sample was rotated by 90°. Had the drift been completely ruled out in the course of the distributed calibration and had the used standard have just insignificant uncertainties, the same coefficients would have been obtained over again with the new position of the sample. And indeed, after the calibration, the coefficients have not changed.

Neither has dependence been detected of the difference in the coefficients upon the step sizes of the net. It is also worth noting that the difference of the coefficients is not only observed in the neighborhood of the origin of coordinates but in other parts of the scanner field and for the whole scanner as well. For instance, the mean values calculated by the whole CDB are as follows: $<\bar{K}_x> = 0.306$ Å, $<\bar{K}_y> = 0.292$ Å (difference 4.6%), $<\alpha> = 0.1^\circ$. Thus, the obtained result shows that the difference between the coefficients is caused by some systematic error which has nothing to do with the standard nor with the method used for compensation of drift influence.

Since the counter-scanned images used for calibration in Ref. [15] were obtained more than 8 years ago (the same pyrographite crystal was used both then and now), a certain degradation of piezoceramics, mechanical or electronic units of the microscope may have probably occurred for such a long period of time. On the one hand, taking into account that $<\bar{K}_x>$ exactly coincided with Δ_x, we could assume that the piezoceramics itself has not changed, since it is hardly possible that exactly half of the scanner has aged while the other one has not. On the other hand, during the raster scanning, the workload of X manipulator is much higher than that of Y manipulator, which could cause the

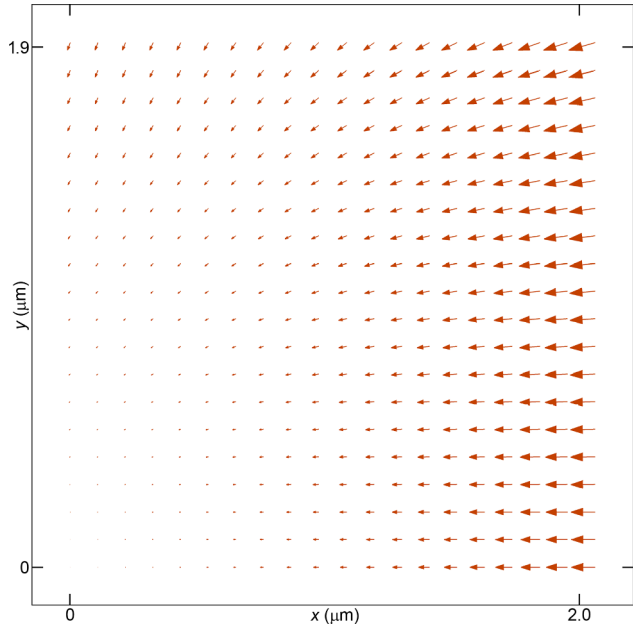

Fig. 4. Static nonlinear distortions of the probe microscope piezoscanner in the lateral plane. The arrows show the value and direction of the distortion. The length of the vector located in the right top corner of the scanner field makes 33 nm. The picture corresponds to the position of scanner Z manipulator moved to the middle of its range.

difference in sensitivities due to the difference in aging rates. The previous operation of the scanner during many years with the similar workload of the manipulators did not lead to any differences in sensitivity between the X and Y manipulators according to the calibration results obtained in Ref. [15]. There were no long breaks in microscope operation [22]. More detailed analysis showed that we most likely observed a disadjustment of electronics of the piezoscanner's Y channel that apparently happened when transporting the instrument.

The comparison of the 2nd order regression surfaces in Figs. 3(a)–(c) obtained in the real mode with the 2nd order regression surfaces in Figs. 3(a)–(c) in Ref. [12] obtained in the virtual mode showed that the surfaces obtained in the real mode are close to planes (vertical scales in these figures are equal). The detected proximity indicates that the main causes of the regression surface bending are distortions caused by thermal drift and creep, which are excluded by FOS methods in the real mode.

If the fact is established that the microscope scanner can be characterized by 1st order regression surfaces (see Figs. 3(a)–(c)), then the subsequent distributed calibrations of this or similar scanners can be substantially simplified. As is known, the position of a plane in space is uniquely defined by coordinates of its three points. Thus, by conducting the distributed calibration in three positions of the scanner field, located as far as possible from each other, the searched for regression planes can be found [23]. To reach the required precision of correction of nonlinearities and spurious couplings, the appropriate number of repetitive calibrations should be carried out in each of the three positions. Since LCCs change very smoothly and the movement range of Z manipulator is usually by an order less than the movement ranges of X, Y manipulators, the search for LCCs can be carried out for, say, five approximately equidistant positions of Z manipulator. Thus, the distributed calibration in the space of scanner movements in that case can be reduced to measurement of LCCs in only 15 points.

2.5. Nonlinear piezoscanner distortions and spurious couplings between manipulators

Replacing the found 2nd order regression surfaces with 1st order regression surfaces (planes) and changing the vertical scales so as the tilts of the regression surfaces are clearly seen, we obtain Figs. 3(d)–(f). The regression surface $\bar{K}_x^r$ (see Fig. 3(d)) is tilted towards the axis x, which points out a nonlinear response of the scanner X manipulator to the driving voltage applied. Besides, the regression surface $\bar{K}_x^r$ is also slightly tilted towards the axis y indicating small nonlinear spurious couplings from other scanner manipulators, in particular, the Y manipulator. As is seen from the figure, the response nonlinearity of the X manipulator noticeably exceeds the nonlinearity due to spurious couplings.

The regression surface $\bar{K}_y^r$ (see Fig. 3(e)) in comparison to the regression surface $\bar{K}_x^r$ has notably less overall tilt (the vertical scales in the figures (d) and (e) are the same), *i.e.*, contribution of Y manipulator to distortions is notably less than the one of X manipulator. It should be noted that the tilt of the regression surface $\bar{K}_y^r$ towards the axis x is comparable with its tilt towards the axis y. This means that with the Y manipulator, the nonlinearities caused by spurious couplings are comparable with piezoceramics nonlinear response. The probable cause of the observed differences between $\bar{K}_x^r$ and $\bar{K}_y^r$ is mechanical and/or material unsymmetry of the particular piezoscanner.

According to Fig. 3(f), the regression surface α^r is located practically horizontal, therefore the dependence of nonorthogonality between the scanner manipulators X and Y on the scanner movements in the lateral plane is negligible. For numerical estimates of static nonlinear scanner distortions, it is convenient to use the maximum differences $\Delta_{\bar{K}_x^r}^{\max} = 0.007$ Å, $\Delta_{\bar{K}_y^r}^{\max} = 0.006$ Å, and $\Delta_{\alpha^r}^{\max} = 0.09°$ of the regression surfaces from the horizontal plane (see Eqs. (13) in Ref. [11]), *i.e.*, the surface into which the regression surfaces would degenerate in case of no distortions.

In order to better understand the degree and the character of the microscope scanner static lateral distortions, a vector field is shown in Fig. 4, where the arrows represent local values and local directions of the revealed nonlinear distortions. The pattern in Fig. 4 corresponds to the case when the entire field 2019.3 × 1907.1 nm is "scanned" according to the raster trajectory of the direct image. Nonlinear raster distortions are determined by formulae (8) given in Ref. [11] by using the joint CDB.

As it was expected, the distortions are negligibly small near the origin of coordinate system of the scanner (supplying voltages are equal to zero) and they increase as the probe approaches the edge of the range, where the measurement error reaches $\Delta_{\bar{K}_x^r}^{\max} 100\% / \bar{K}_x^r(0,\ 0) = 2.3\%$. The size of the longest vector in Fig. 4 (located in the right top corner of the field) makes 33.4 nm which is about 1.7% of the scanner field side. The obtained error values show that the contribution of nonlinearities and spurious couplings to the total raster distortion is several times less than the contribution from thermal drift and creep which makes 8–11% (see Refs. [12,15]). It can be clearly seen in Fig. 4 that the vectors originating from points on the y axis are located at some angle to this axis pointing out the existence of a small nonorthogonality ($<\alpha> = 0.1°$) [15]. The nonorthogonality is equal to the angle at which those vectors are seen from the origin of coordinates [1].

To determine the residual lateral error of the distributed calibration method, root-mean-square deviations of LCCs are found by formulae (14) given in Ref. [11]: $\sigma_{\bar{K}_x} = 0.025$ Å, $\sigma_{\bar{K}_y} = 0.026$ Å ($\sigma_\alpha = 1.1°$). Taking into account the number n of LCSs in the obtained CDB, the estimated error of regression LCCs could make $\sigma = 3\sigma_{\bar{K}_x}/\sqrt{n} = 0.0002$ Å (3σ). The error σ is numerically an order of magnitude less than the amplitude of thermal motions of carbon atoms in graphite lattice sites at room temperature [24].

2.6. Errors caused by defects of the standard surface. Automatic characterization of a crystal surface

Since a crystal lattice is used for LCC determination, an additional error is introduced in the LCCs because of a variation of the lattice constant caused by random imperfections of the standard. Another

component of the error σ is noises of the registration and positioning systems of the STM. With CDB as large as $n = 90000$ LCSs, the error $\sigma_a = \sigma a/<\bar{K}_x> = 0.002$ Å (3σ) of STM-measurement of graphite lattice constant a, caused by the error σ of scanner calibration, becomes comparable with the measurement error of graphite lattice constant by X-ray diffraction or neutron diffraction methods [16]. Unlike the last two methods, where the lattice constant is mainly measured within the crystal volume, the suggested method enables accurate measurement of the lattice constant exclusively on the surface.

In different locations of the scanner field, the LCC root-mean-square deviations are numerically close to each other and to the LCC root-mean-square deviations $\sigma_{\bar{K}x}$, $\sigma_{\bar{K}y}$ determined for the whole field of the scanner. The relations detected point out that in spite of localization of the defect in graphite, random changes of the graphite lattice constant are most likely small and the main part of the errors $\sigma_{\bar{K}x}$, $\sigma_{\bar{K}y}$ relates to the noise components of the registration and the positioning systems of the used microscope.

Graphite lattice can have small variations of sizes in different places of the crystal surface or in the same place before and after cleavage. Those variations were numerically estimated by comparing the LCCs $\bar{K}1_x$, $\bar{K}2_x$ ($\bar{K}1_y$, $\bar{K}2_y$) from CDB that corresponded to the same area of the scanner field (in Fig. 1, one of such areas is outlined with a triple frame) but had been taken either in different places 1 and 2 of the standard or in the same place but on different cleavages 1 and 2. This approach eliminates the influence of the scanner nonlinearities and allows the relative change δ_a of the lattice constant to be estimated by the relative change $\delta_{\bar{K}x} = 2|\bar{K}1_x - \bar{K}2_x|100\%/(\bar{K}1_x + \bar{K}2_x)$ (or $\delta_{\bar{K}y}$) of the LCC. For the lattice constant located in parallel to X manipulator, $\delta_a = \delta_{\bar{K}x}$; for the lattice constant located in parallel to Y manipulator, $\delta_a = \delta_{\bar{K}y}$.

A preliminary analysis has shown that the relative change in constant lattice δ_a on the surface of the pyrographite crystal in use makes $\delta_{\bar{K}x} \approx \delta_{\bar{K}y} = 0.8\%$ which is 5 times higher than in the volume of natural single crystal graphite [16]. Thus, the method suggested enables not only for scanner calibration but also for estimating errors of the standard itself. Matching $\sigma_{\bar{K}x} = 0.025$ Å with the difference $\bar{K}1_x - \bar{K}2_x = 0.003$ Å confirms the earlier made assumption that random changes in the pyrographite lattice constant are insignificant in comparison with the noise components of the registration and the positioning systems. Because of the importance of the issue of invariability of HOPG crystal lattice constant, a special study is to be conducted in order to cover the issue in detail.

By saving the relative coordinates of B and C features (skippings A ↔ B, A ↔ C) found during the calibration, it is easy to obtain a distribution of crystal lattice constants and angles between crystallographic directions over the sample surface [23]. Thus, beside calibration, the developed method can also be used for characterization of crystal surfaces, localization of surface/subsurface defects, mechanical stresses, studying superstructures (superlattices) [25], surface reconstructions, adsorption/desorption processes, *etc*. In particular, by a small periodical modulation of sizes of unit cells, low contrast superstructures [25] could be discovered, which is hard or impossible by using other methods.

When implementing the surface characterization, instead of rigid binding of the net to the absolute coordinates of the scanner; it is necessary to calculate each next absolute net position relative to the position of the feature A determined in the end of the last skipping cycle A ↔ C (see inset in Fig. 2(b)). In this case, the microscope probe will drift along with the surface exactly like in FOS [14,25,26] and it will never leave the limits of the crystal area under characterization.

3. Discussion

At present, microscopes equipped with a closed-loop positional system are unable to measure surface topography with high resolution because of noises of the linear position sensors. To operate microscope near or at the utmost resolution, the closed-loop positional system has to be turned off. As a result, the measured topography is distorted by drifts, nonlinearities, and spurious couplings of the scanner manipulators.

To correct the errors caused by the manipulators' nonlinearities and spurious couplings, with the closed-loop positional system turned on, a sort of distributed scanner calibration is carried out by the standards which do not require the utmost resolution of the microscope [9,10]. The data obtained during such distributed calibration, which describe the nonlinear scanner behaviour, are used later to correct the topography measured with a high resolution.

The fundamental distinction of the suggested distributed calibration method is that the random velocity fluctuations of the drift thermal component have no influence on the obtained LCCs. Moreover, the error of LCC determination can be substantially reduced by performing repeated scanner calibrations the number of which has no principle restrictions. Unlike the closed-loop positional system, the developed calibration approach does not introduce any additional noise which permits calibrating the scanner by natural references such as constants of crystal lattices, using separate atoms and interstitials as features.

Thermal drift of a microscope can be decreased by means of microscope temperature stabilization in a special thermally-stabilized box or room. The drawback of temperature stabilization is that equalizing the temperature of different parts of the instrument takes a rather long time and cannot be done completely because of the presence of varying heat sources inside the microscope. Temperature stabilization of the microscope at a low temperature (2–20 K) makes it possible to further reduce the thermal drift rate and achieve high mechanical stability of the tunnel gap [27]. However, cooling to a low temperature would greatly complicate the experiment and increase its conduction time. Moreover, the cryogenic probe microscope is a much less universal instrument as compared with regular microscopes, which substantially restricts its application area.

Due to the built-in mechanism of *in situ* compensation of drift influence [11], the distributed calibration and the crystal surface characterization can be performed by the suggested method in nanometer and subnanometer scales at room temperature without special temperature stabilization of the instrument. Not high mechanical stability of the tunneling gap at the room temperature is compensated by the possibility of the calibration method to perform multiple repeated measurements.

4. Conclusion

The use of the atomic surface of a crystal as a standard surface allows obtaining LCC distribution of a very high density. However, at present it is impossible to cover the whole scanner's movement range with such a dense net, especially at several levels, because of low performance of the existing microscopes. The results obtained in the course of real distributed calibration show that the dense net should not necessarily be used. For example, to acquire an adequate CDB, it is enough to perform calibration only in three points of the scanner field for each of 3–5 equidistant positions of the Z manipulator.

The key points of the research can be summarized as follows:

(1) Operability of the distributed calibration method built on the base of feature-oriented approach has been confirmed.
(2) Feasibility of accurate calibration of the probe microscope scanner by a crystal lattice of highly oriented pyrolytic graphite at room temperature has been proved.

Acknowledgments

The work was supported by the Ministry of Education and Science of the Russian Federation (contract 14.575.21.0149, project ID RFMEFI57517X0149). Equipment provided by the MIET Core Facilities "MEMS and electronic components" was used during the

measurements. I thank O.E. Lyapin, Assoc. Prof. S.Y. Vasiliev, and L.B. Sharova for their critical reading of the manuscript; Dr. A.L. Gudkov, Prof. E.A. Ilyichev, Assoc. Prof. E.A. Fetisov, Assoc. Prof. N.A. Djuzhev and late Prof. E.A. Poltoratsky for their support and encouragement.

References

[1] R.V. Lapshin, Automatic lateral calibration of tunneling microscope scanners, Rev. Sci. Instrum. 69 (1998) 3268–3276. Available from: www.niifp.ru/staff/lapshin/en/#articles.
[2] V.Y. Yurov, A.N. Klimov, Scanning tunneling microscope calibration and reconstruction of real image: drift and slope elimination, Rev. Sci. Instrum. 65 (1994) 1551–1557.
[3] R. Staub, D. Alliata, C. Nicolini, Drift elimination in the calibration of scanning probe microscopes, Rev. Sci. Instrum. 66 (1995) 2513–2516.
[4] J. Garnaes, L. Nielsen, K. Dirscherl, J.F. Jørgensen, J.B. Rasmussen, P.E. Lindelof, C.B. Sørensen, Two-dimensional nanometer-scale calibration based on one-dimensional gratings, Appl. Phys. A 66 (1998) S831–S835.
[5] R.V. Lapshin, Analytical model for the approximation of hysteresis loop and its application to the scanning tunneling microscope, Rev. Sci. Instrum. 66 (1995) 4718–4730. Available from: www.niifp.ru/staff/lapshin/en/#articles.
[6] R.V. Lapshin, An improved parametric model for hysteresis loop approximation, arXiv:1701.08070, 2018, 25 pp. Available from: arxiv.org/abs/1701.08070.
[7] K. Dirscherl, J. Garnæs, L. Nielsen, J.F. Jørgensen, M.P. Sørensen, Modeling the hysteresis of a scanning probe microscope, J. Vac. Sci. Technol. B 18 (2000) 621–625.
[8] D.A. Chernoff, J.D. Lohr, High precision calibration and feature measurement system for a scanning probe microscope, US Patent 5,825,670, 1998.
[9] D.R. Marshall, Optical position sensor with corner-cube and servo-feedback for scanning microscopes, US Patent 5,196,713, 1993.
[10] V. Elings, Scan control for scanning probe microscopes, US Patent 5,557,156, 1996.
[11] R.V. Lapshin, Drift-insensitive distributed calibration of probe microscope scanner in nanometer range: approach description, Appl. Surf. Sci. 359 (2015) 629–636. Available from: www.niifp.ru/staff/lapshin/en/#articles.
[12] R.V. Lapshin, Drift-insensitive distributed calibration of probe microscope scanner in nanometer range: virtual mode, Appl. Surf. Sci. 378 (2016) 530–539. Available from: www.niifp.ru/staff/lapshin/en/#articles.
[13] P. Klapetek, D. Nečas, A. Campbellová, A. Yacoot, L. Koenders, Methods for determining and processing 3D errors and uncertainties for AFM data analysis, Meas. Sci. Technol. 22 (2011) 025501.
[14] R.V. Lapshin, Feature-oriented scanning methodology for probe microscopy and nanotechnology, Nanotechnology 15 (2004) 1135–1151. Available from: www.niifp.ru/staff/lapshin/en/#articles.
[15] R.V. Lapshin, Automatic drift elimination in probe microscope images based on techniques of counter-scanning and topography feature recognition, Meas. Sci. Technol. 18 (2007) 907–927. Available from: www.niifp.ru/staff/lapshin/en/#articles.
[16] P. Trucano, R. Chen, Structure of graphite by neutron diffraction, Nature 258 (1975) 136–137.
[17] E.P. Stoll, Restoration of STM images distorted by time-dependent piezo driver aftereffects, Ultramicroscopy 42–44 (1992) 1585–1589.
[18] Y. Peng, T. Cullis, G. Möbus, X. Xu, B. Inkson, Conductive nichrome probe tips fabrication, characterization and application as nanotools, Nanotechnology 20 (2009) 395708.
[19] M.-S. Wu, Y.-P. Lin, C.-H. Lin, J.-T. Lee, Formation of nano-scaled crevices and spacers in NiO-attached graphene oxide nanosheets for supercapacitors, J. Mater. Chem. 22 (2012) 2442–2448.
[20] C.A. Clifford, M.P. Seah, Simplified drift characterization in scanning probe microscopes using a simple two-point method, Meas. Sci. Technol. 20 (2009) 095103.
[21] F. Marinello, M. Balcon, P. Schiavuta, S. Carmignato, E. Savio, Thermal drift study on different commercial scanning probe microscopes during the initial warming-up phase, Meas. Sci. Technol. 22 (2011) 094016.
[22] R.S. Howland, The scanning probe microscope as a metrology tool, in: S.H. Cohen, M.T. Bray, M.L. Lightbody (Eds.), Atomic Force Microscopy/Scanning Tunneling Microscopy, Plenum Press, New York, 1994, pp. 347–358 453 pp.
[23] R.V. Lapshin, Productive drift-insensitive distributed calibration of probe microscope scanner in nanometer range, in: Proc. 26th Russian Conference on Electron Microscopy, vol. 1, Zelenograd, Russian Federation, 2016, pp. 268–269, Available from: www.niifp.ru/staff/lapshin/en/#reports (in Russian).
[24] R. Chen, P. Trucano, Comparisons of atomic thermal motions for graphite at 300 K based on X-ray, neutron, and phonon-spectrum data, Acta Cryst. A 34 (1978) 979–982.
[25] R.V. Lapshin, Observation of a hexagonal superstructure on pyrolytic graphite by method of feature-oriented scanning tunneling microscopy, in: Proc. 25th Russian Conference on Electron Microscopy, vol. 1, Chernogolovka, Russian Federation, 2014, pp. 316-317, Available from: www.niifp.ru/staff/lapshin/en/#reports (in Russian).
[26] R.V. Lapshin, Feature-oriented scanning probe microscopy, in: H.S. Nalwa (Ed.), Encyclopedia of Nanoscience and Nanotechnology, American Scientific Publishers, 2011, pp. 105–115. Available from: www.niifp.ru/staff/lapshin/en/#articles.
[27] J.D. Hackley, D.A. Kislitsyn, D.K. Beaman, S. Ulrich, G.V. Nazin, High-stability cryogenic scanning tunneling microscope based on a closed-cycle cryostat, Rev. Sci. Instrum. 85 (2014) 103704.